RESEARCH ARTICLE

Insight into metal binding properties of biochar-derived DOM using EEM-PARAFAC and differential absorption spectra combined with two-dimensional correlation spectroscopy

Xiaoli Zhang[1] · Xuewei Cai[1] · Zhaowei Wang[1] · Xing Yang[1] · Shan Li[1] · Guiwei Liang[1] · Xiaoyun Xie[1]

Abstract

A large amount of biochar-derived dissolved organic matter (BDOM) will be released into the environment with biochars application into repairing soil/water, which may alter the fate and transport of contaminants. In this study, four DOM samples were extracted from cauliflower root biochar (CRBC), reed straw biochar (RSBC), corn stalks biochar (CSBC), and potato stalk biochar (PSBC). Excitation-emission matrix combined with parallel factor (EEM-PARAFAC) analysis, differential absorbance spectra (DAS), and two-dimensional correlation spectroscopy (2D-COS) analysis were applied to explore the complexation property of BDOM with metals. DAS showed sites heterogeneity within the DOM pool for metals complexing. Humic-like and fulvic-like substances were main fluorescent components identified by EEM-PARAFAC. 2D-COS analysis revealed that polysaccharides and aliphatic firstly responded to Pb(II) binding with CRBC-derived DOM and three other biochar-derived DOM, respectively. While aliphatic groups, aromatic N=O, and polysaccharides gave the fastest response to Cu(II) binding with CRBC, RSBC, and the other two biochar-derived DOM, respectively.

Keywords Biochar-derived DOM · Heavy metals · Differential absorption spectra · EEM-PARAFAC · Two-dimensional correlation spectroscopy

Introduction

Heavy metals pollution that resulted from rapid industrialization and urbanization has become a serious issue (Zhao et al. 2015; Huang et al. 2019) due to its persistence and non-biodegradability in the environment (Tang et al. 2019a, b). Thus, control and repair of heavy metals contamination to improve environmental quality is of utmost necessity. Many conventional technologies including physical, chemical, and biological methods have been used for the removal of heavy metals from the soil and aquatic system in the past decades (Feng et al. 2020; Li et al. 2017a). In recent years, using

biochars to repair contaminated soil or water has been considered to be the valid, prospective, and widely used method for its high efficiency, low cost, and environmental sustainability (Mohan et al. 2014). It has been reported that the addition of biochars to soil can ameliorate soil quality and fertility; increase soil nutrients, water holding capacity, and crop yield (Abel et al. 2013; Jin et al. 2016); and repair heavy metals polluted soils (Huang et al. 2019; Liu et al. 2019; Zhai et al. 2018). Several reports also suggested the strong sorption ability of biochars for many kinds of contaminants (e.g., heavy metals and pharmaceuticals) from water and waste water (Li et al. 2017a; Zhang et al. 2013).

Biochars, the carbonaceous materials, are prepared from the thermal pyrolysis of organic biomass (e.g., forestry wastes, industrial organic wastes, and agricultural wastes) under oxygen-limited conditions (Huang et al. 2019; Liu et al. 2018; Yang et al. 2019). Due to its tremendous specific area, multihole structure, abundant surface functional groups, and high cation exchange capacity, which are intently associated to the origins of biochars and also obviously relied on thermal pyrolysis conditions (Eykelbosh et al. 2015; Li et al. 2017a; Jin et al. 2018; Li et al. 2018), biochars have been widely

---

Responsible Editor: Zhihong Xu

✉ Zhaowei Wang
wangzw@lzu.edu.cn

[1] Gansu Key Laboratory for Environmental Pollution Prediction and Control, College of Earth and Environmental Sciences, Lanzhou University, Tianshui South Road 222, Lanzhou 730000, Gansu, China

studied and applied into the removal of the various organic contaminants and heavy metal pollutants. Noteworthily, a large amount of biochar-derived DOM (BDOM) will be released into the soil or water system while getting the advantages of biochar utilization (Huang et al. 2019; Li et al. 2017b), which may be the key influencing factor affecting the application potentiality of biochars. The main reason is the complexation between BDOM and heavy metals (Yuan et al. 2017; Xu et al. 2019; Guo et al. 2019; Chen et al. 2015; Huang et al. 2018a). BDOMs, the easily extractable and mineralizable carbon fraction released from biochars, are compound and heterogeneous mixtures of aromatic and aliphatic carbon structure (Huang et al. 2019; Zhao et al. 2019; Li et al. 2017b). It can straightly interact with metals for its high aromaticity and plentiful organic functional groups like carboxylic, phenolic, aliphatic, hydroxyl, carbonyl, and quinones with high active sites (Karami et al. 2011; Huang et al. 2019). The interaction of BDOM with heavy metals has been demonstrated to alter the mobility, distribution, and speciation of metals, thus the bioavailability and toxicity of heavy metals in soil or water system are changed (Zhao et al. 2013; Li et al. 2018; Beesley et al. 2014; Soja et al. 2017). The binding characteristics between BDOM and heavy metals are mainly relied on the chemical structures and compositions of BDOM which are controlled by the material sources and pyrolysis conditions like temperature and residence time (Li et al. 2018; Liu et al. 2019) and reaction conditions such as pH and temperatures (Huang et al. 2019; Xu et al. 2018).

Many technologies are used to investigate the binding characteristics between DOMs and heavy metals, including size exclusion chromatography (SEC), nuclear magnetic resonance (NMR) spectroscopy, X-ray absorbance spectroscopy (XAS), low- and high-resolution mass spectrometry, and others (Xiao et al. 2019; Lu et al. 2017; Huang et al. 2018b). However, these methods require much higher concentration of the goal metals and DOM. The chemical and physical properties and structures of DOM are inevitably altered during the sample preparations. By comparison, spectroscopic analyses such as absorbance and fluorescence methods are applied for the complexation between DOM and metals due to its nondestructivity, sensitivity, and fast and simple operation (Lu et al. 2017). Ultraviolet-visible (UV-vis) absorption, differential absorption spectra (DAS) analysis, excitation-emission matrices (EEMs) combined with parallel factor (PARAFAC) analysis, and two-dimensional correlation spectroscopy (2D-COS) analysis would be the valid research methods (Tang et al. 2016; Yuan et al. 2017). Additionally, synchronous fluorescence (SF) spectroscopy and Fourier transform infrared (FTIR) spectrum can show the detailed information of fluorescent fractions and functional groups in DOM-metals, respectively (Huang et al. 2019; Xu et al. 2018). However, the peaks of FTIR and SF spectroscopy often overlapped as a result of the heterogeneity of DOMs. Recent researches

suggested that 2D-COS analysis can help solve the problem of peaks overlapping and provide the order of structure changes of DOMs in response to external perturbations (e.g., the concentrations of metals) (Xu et al. 2018; Chen et al. 2019). Moreover, heterospectral 2D-COS can reveal an in-depth information about the correlation on the structural response of the system to the perturbation (Yu et al. 2011; Chen et al. 2015; Chen et al. 2019). And hetero-2DCOS analysis usually integrates spectral signals under the same external perturbation (Chen et al. 2019; Kim et al. 2006).

In this study, two heavy metals (Pb(II) and Cu(II)) and four BDOM (CRDOM, RSDOM, CSDOM, and PSDOM) obtained from different biomass were selected to explore the complexation mechanism of BDOM with heavy metals. The EEM-PARAFAC, DAS, and 2D-COS analysis on UV-vis, SF, and FTIR spectra were used to evaluate the different binding characteristics for CRDOM/RSDOM/CSDOM/PSDOM-Pb(II)/Cu(II) interactions. The specific objectives of this work include: (i) identifying and determining the components of BDOM obtained from different sources by using EEM-PARAFAC, (ii) calculating the binding parameters of Pb(II) and Cu(II) with BDOMs by employing the Stern-Volmer equation and comparing the binding ability of different sources BDOM with heavy metals, and (iii) exploring the Pb(II) and Cu(II) binding characteristics of different BDOMs using DAS and 2D-COS combined with UV-vis, SF and FTIR, and heterospectral two-dimensional SF-FTIR correlation analysis.

Materials and methods

Biochar preparation

The biochars applied in this study were obtained from agricultural residues of cauliflower root, corn straw, and potato stalk collected from suburb and reed straw obtained from the edge of the Yellow River of Lanzhou (Gansu, China). They were rinsed with distilled water, dried at 60 °C, and crushed to sieve through a 20-mesh screen. The crushed biomass was placed in ceramic crucibles with lids and wrapped with aluminum foil and put in a muffle furnace for pyrolysis with the temperature rising to 500 °C and maintained for 6 h under the oxygen-limited condition, and then cooling to room temperature. Afterward, the biochars were ground and sieved through a 100-mesh screen, finally stored at a dry and dark place for the later experiment.

DOM samples

Before the extraction experiment began, the biochars were dried at 80 °C for 1 h. The method of extraction experiment of BDOM is as depicted by previous studies (Huang et al.

2018a; Hu et al. 2016). In short, CRBC, RSBC, CSBC, and PSBC were extracted with ultrapure Milli-Q water and the solid/liquid ratio of 1/20 (*w/v*) was used in this study. Mixed liquids were shaken at 25 °C and 250 rpm for 24 h in darkness. After centrifuging at 4000 rpm for 25 min, the supernatants were filtered through a 0.45-μm glass fiber filter. Finally, the filtrates were stored at 4 °C for utilizing in the later experiments.

Quenching titration

BDOM concentrations were diluted to around 10 mg/L to decrease the inner filter effects before quenching titration (Xu et al. 2013). And the pH values of the primitive extracts were adjusted to 6.0 ± 0.2 by 0.1 M HNO_3 and NaOH solutions. Metal titrations were carried out by adding 0.01 M $Pb(NO_3)_2$ or 0.01 M $Cu(NO_3)_2$ titrants to each of BDOM solutions. The concentration range of Pb(II) and Cu(II) in the BDOM solutions was set as 0 to 140 μM (0, 10, 20, 30, 40, 50, 60, 80, 100, 120, 140 μM). The titrant volume was added no more than 5% of the solution volume to avoid the concentrations effect (Guo et al. 2019). Subsequently, to guarantee reaction equilibrium, all titrated BDOM solution samples were shaken for 6 h at 250 rpm and 25 °C in dark conditions. All experiments were performed in glass bottles. Finally, these solution samples were analyzed by UV-vis, EEM, and SF spectroscopy. A series of solutions containing undiluted DOM samples of the same proportion of heavy metals were prepared and then freeze-dried for FTIR spectroscopy.

Spectral determination

UV-vis absorption spectra of the BDOM solutions were determined at wavelengths ranging from 200 to 700 nm by employing an UV-vis spectrophotometer (UNICAM Evolution UV300) with 10 mm rectangular cuvettes at room temperature.

EEMs spectrum of the titrated solutions were determined by a Cary Eclipse Spectrometer (United States Varian China Ltd.) at room temperature. The parameters of fluorescence measurement were set as follows: emission (Em) wavelengths were 250–550 nm, excitation (Ex) wavelengths were 200–450 nm, slit width was 5 nm, scan rate = 2400 nm/min, and voltage = 600 V; the ultrapure Milli-Q water was used as blank.

SF spectra was scanned with 5-nm emission and excitation scanning intervals and a constant offset ($\Delta\lambda = 60$ nm) at room temperature, the range of wavelength was set as 250–550 nm, and the ultrapure water was used as blank to command solutions for each of titrated BDOM samples (Lawaetz and Stedmon 2009; Guo et al. 2019).

FTIR spectrum was used to analyze the freeze-dried BDOM samples. FTIR spectrum which ranged from 4000 to 400 cm^{-1} was obtained by applying 2 mg of BDOM powder and a FTIR spectrometer (Nexus 670, Thermo-Nicolet, USA).

DAS analysis of UV-vis absorbance

Because original spectra usually has no features, to enhance the spectra resolution, DAS including zero-order and log-transformed differential spectrum (Xu et al. 2018; Yan et al. 2013; Gao et al. 2015a; Gao et al. 2015b) were used in this work.

The zero-order and log-transformed differential spectrum equations were presented as Eq. (1) and Eq. (2):

$$DA_\lambda = A_{\lambda,i} - A_{\lambda,ref} \tag{1}$$

$$DlnA_\lambda = lnA_{\lambda,i} - lnA_{\lambda,ref} \tag{2}$$

In the above formula, DA_λ and $DlnA_\lambda$ are the differential absorbance of zero-order and log-transformed spectrum at wavelength λ, respectively. $A_{\lambda,i}$ and $A_{\lambda,ref}$ are absorbance intensities determined at wavelength λ at the selected metal concentration and an appropriate reference concentration (e.g., without metals addition in this study), respectively.

PARAFAC analysis and complexation modeling

PARAFAC is applied to simulate the dataset of EEMs. Complex mixtures of DOM fluorophores can be statistically decomposed into fractions related to its spectral number or shape by PARAFAC, and to estimate the true underlying EEMs spectra (Wang et al. 2013). In this work, the DOMFluor toolbox (www.models.life.ku.dk) in MATLAB R2017b was used to PARAFAC analysis, which was calculated by utilizing two to 10 component patterns and conducted with non-negativity constraints, and the correct numbers of fluorescence component were produced by split-half analysis, residual analysis, visual examination, sum of squared error, explained variance, and core consistency. The relative levels of individual fluorescent components can be evaluated by the maximum fluorescence intensity (Fmax) (R.U.) obtained by PARAFAC analysis (Huang et al. 2018a). The detailed information about PARAFAC analyses has been depicted in previous studies (Li et al. 2017a; Yuan et al. 2015). In this study, 44 EEMs samples were included in each different BDOM PARAFAC analysis.

Date analysis

The binding parameters of Pb(II) and Cu(II) with PARAFAC-derived fractions were investigated by the Stern-Volmer equation (Gu et al. 2015; Ferrie et al. 2017; Zhao et al. 2019).

The Stern-Volmer equation was calculated as Eq. (3):

$$\frac{F_0}{F} = K_b C_M + 1 \tag{3}$$

where F_0 is the original fluorescent intensity (without metals addition) and F is the intensity scores of fluorescent components at the metal concentration C_M. K_b is the Stern-Volmer quenching constant of fluorescence components of Pb(II) and Cu(II).

2D-COS analyses

2D-COS analyses of the UV, SF, and FTIR were carried out applying a series of concentration gradients of adding metals as external perturbations. The application of synchronous and asynchronous spectrum of 2D-COS analysis can provide the complexation extent and sequence between metal ions and DOM functional groups (Noda and Ozaki 2004). A more exhaustive description of the 2D-COS theory and principle has been depicted in previous studies (Chen et al. 2015; Chen et al. 2019; Hur and Lee 2011; Ozaki et al. 2001). All of the calculation and drawing functions of the 2D-COS analysis were performed utilizing the "2D Shige" software (Kwansei Gakuin University, Japan).

Results and discussion

Characteristics of BDOM

The DOC concentrations of BDOM solutions were determined by a TOC analyzer (Elementar vario TOC select). The quantity of BDOM released from the different biochars was shown in Table S1. The DOC concentrations increased in the order of RSBC (11.41) < PSBC (31.21) < CSBC (113.91) < CRBC (118.20). For BDOMs, the CRDOM solution had dark-yellow color, the CSDOM solution had light-yellow color, and the PSDOM and RSDOM solutions had no obvious colors (Fig. S1). The visual appearances of the extracted DOC solutions were usually correlated with the DOC measurements (Liu et al. 2019). The CRDOM and CSDOM had higher DOC concentrations and darker colors than those of PSDOM and RSDOM.

The analyses of SUVA$_{254}$ (the specific UV absorption at 254 nm) and S$_R$ (the ratio between the absorbance slop from 275 to 295 nm divided by the slop from 350 to 400 nm) were used to further study the characteristics of BDOM (Table S1) (Li et al. 2017b). The average of SUVA$_{254}$ of BDOM was 5.07–15.59 L mg C^{-1} m^{-1}, and indication of a higher aromaticity. The sequence of the four biochars' aromaticity was CRBC > PSBC > CSBC > RSBC. The S$_R$ parameters of BDOMs ranged at 1.08–1.46. S$_R$ values had an inverse

relationship with the molecular weight of BDOM (Xiao et al. 2013). The result indicated that the four biochars had a low molecular, and the molecular size order was RSBC > CSBC > CRBC > PSBC.

The additional fluorescence index (FI) and humification index (HIX) were obtained from EEMs data to understand the source of BDOM samples (Table 1). The FI > 1.4 and < 1.3 indicated the terrestrial and microbial sources, respectively (Xu et al. 2019). In this work, the FI of RSBC (1.075) was lower than that of others (1.863–2.332). The result suggested that RBDOM originated mainly from terrestrial runoff and others mainly from microbial sources. The HIX of RSDOM (2.527) and CSDOM (0.648) were lower than CRDOM (19.318) and PSDOM (8.728), indicating CRDOM and PSDOM with higher degree of humification.?]

The complexation of BDOM with Pb(II) and Cu(II) as revealed by DAS

UV-vis absorption spectroscopy is an effective method to investigate the feature of DOMs with several spectral parameters and the binding property between DOMs and heavy metals (Huang et al. 2019). Furthermore, though the zero-order spectroscopy is featureless, the DAS including differential zero-order and log-transformed spectroscopy can increase the spectra resolution and investigate the further heterogeneities caused by metals addition in binding sites among different chromophores (Xu et al. 2018; Gao et al. 2015a; Lu et al. 2017).

The intensity of UV-vis absorption dropped near-exponentially with increasing wavelength (Fig. S2), and changes of spectra were broad and featureless with the Pb(II) and Cu(II) addition, possibly owing to the overlapping absorption peaks of the multiple chromophores. The result was similar with the previous studies of metal-DOM interactions (Xu et al. 2018; Guo et al. 2019; Gao et al. 2015a). In order to improve the spectra resolution, DAS including zero-order and log-transformed differential absorption spectra were used and normalized by DOC to reveal that the complexation heterogeneity of BDOM with heavy metals was only associated with the intrinsic properties of BDOM samples. DOC normalized DAS showed obvious metal-active chromophores compared to the original spectra. In the case of Pb(II), the normalized zero-order DAS showed that there were two main types of metal-active chromophores with peaks at 202 and 240 nm for CRDOM-Pb, 208 and 272 nm for RSDOM-Pb, 208 and 271 nm for PSDOM-Pb, and one main peak at 208 nm for CSDOM-Pb (Fig. 1). The intensity of all the peaks enhanced with gradual increase of metal concentrations, but with a great increase extent at the shorter wavelength than the longer wavelength. This suggested that BDOM chromophores at shorter wavelength (e.g., 202, 208, and 240 nm) had a greater participation with metals complexation than those at

**Table 1** Characteristics of the components identified by EEM-PARAFAC analysis

Origin	Component	Ex/Em (nm)	Fluorescent compound	Ref.
CRBC	C1	270/400	Humic-like substance	Park and Snyder 2018
	C2	325/415	Humic-like substance	Xu et al. 2019
	C3	235,300,395/480	Fulvic-like substance; humic-like substance (slight)	Park and Snyder 2018; Chen et al. 2003
	C4	310,245,205/360	Fulvic-like substance	Park and Snyder 2018
RSBC	C1	245/375	Fulvic-like substance	Chen et al. 2003
	C2	200/250–550	Protein-like substance; fulvic-like substance (slight)	Xu et al. 2019; Li et al. 2017a, b
	C3	310/425,545	Humic-like substance;	Xu et al. 2018; Huang et al. 2018a, b
	C4	225,425/505	Fulvic-like substance; humic-like substance (slight)	Chen et al. 2003
CSBC	C1	290/380	Humic-like substance	Li et al. 2017a, b
	C2	310/415	Humic-like substance	Tang et al. 2019a, b
	C3	310/420	Humic-like substance	Huang et al. 2019
	C4	305/355,480	Humic-like substance	Xu et al. 2019; Tang et al. 2019a, b
PSBC	C1	250/395	Fulvic-like substance	Park and Snyder 2018
	C2	275,335/420	Humic-like substance	Tang et al. 2019a, b; Li et al. 2017a, b
	C3	230,395/470	Fulvic-like substance; humic-like substance	Tang et al. 2019a, b; Chen et al. 2003; Li et al. 2017a, b
	C4	200/250–550	Protein-like substance; fulvic-like substance (slight)	Xu et al. 2019; Park and Snyder 2018

longer wavelength (e.g., 272 and 271 nm). The position of wavelength at 202 nm (CRBC) and 208 nm (RSBC, CSBC, and PSBC) was also displayed to a slight shift towards a longer wavelength with the increase of metal concentrations indicated that there was an interaction of BDOM with metals, and addition of metals could result in micro-environmental changes of chromophores groups in BDOM. Compared to Pb(II), the zero-order DAS for BDOM induced by Cu(II) binding had the similar peaks (Fig. S4), which indicated that BDOM had similar binding sites and affinities to Pb(II) and Cu(II) binding.

Since the zero-order spectra usually showed the near-exponential pattern, their log-transformed spectrum can provide the changes of peaks/bands with the metals addition. As expected, the log-transformed spectrum almost performed a liner decrease with the wavelength increase, and there are more areas (e.g., for CRBC, < 233 nm, 233–304 nm, and > 304 nm) wherein the changes of the slopes can be observed (Fig. S3), indicating that the distribution of the functional groups and active sites is uneven. The results suggested the obvious precedence of log-transformed spectrum in the performance of BDOM site specificity for metals complexation

(Xu et al. 2018). In order to obtain more details of the site heterogeneity, log-transformed DAS after additions of Pb(II) and Cu(II) were obtained and shown in Fig. 1 and Fig. S4, respectively. The obtained DAS could show the presence of multiple features that revealed many major peaks/bands to compare with the log-transformed absorption spectra. Addition of Pb(II) and Cu(II) caused a slight increase of intensity of all peaks/bands but with different extent (e.g., CRBC of Fig. 1, three peaks located at 240, 324, and 400 nm), and also indicated that these chromophores have the sensitivity heterogeneity in metal binding (Xu et al. 2018). The weak peaks at 270–400 nm can be found in log-transformed DAS, suggesting that organic compounds contain the chromophores with nonbinding electrons. For example, the λ_{max} of the n-π* transition for ethyl acetoacetate is at about 275 nm, and α, β–unsaturated carboxylic acid is at about 260–280 nm (Guo et al. 2019). Therefore, although zero-order spectra induced by metal were featureless, DAS including zero-order and log-transformed differential spectrum can provide more binding heterogeneities information of BDOM chromophores (i.e., sites distribution, sensitivity, and complexation degree).

Fig. 1 Changes of dissolved organic carbon (DOC) normalized differential spectra and DOC normalized differential log-transformed spectra of biochar-derived DOM samples with increasing Pb(II) concentration
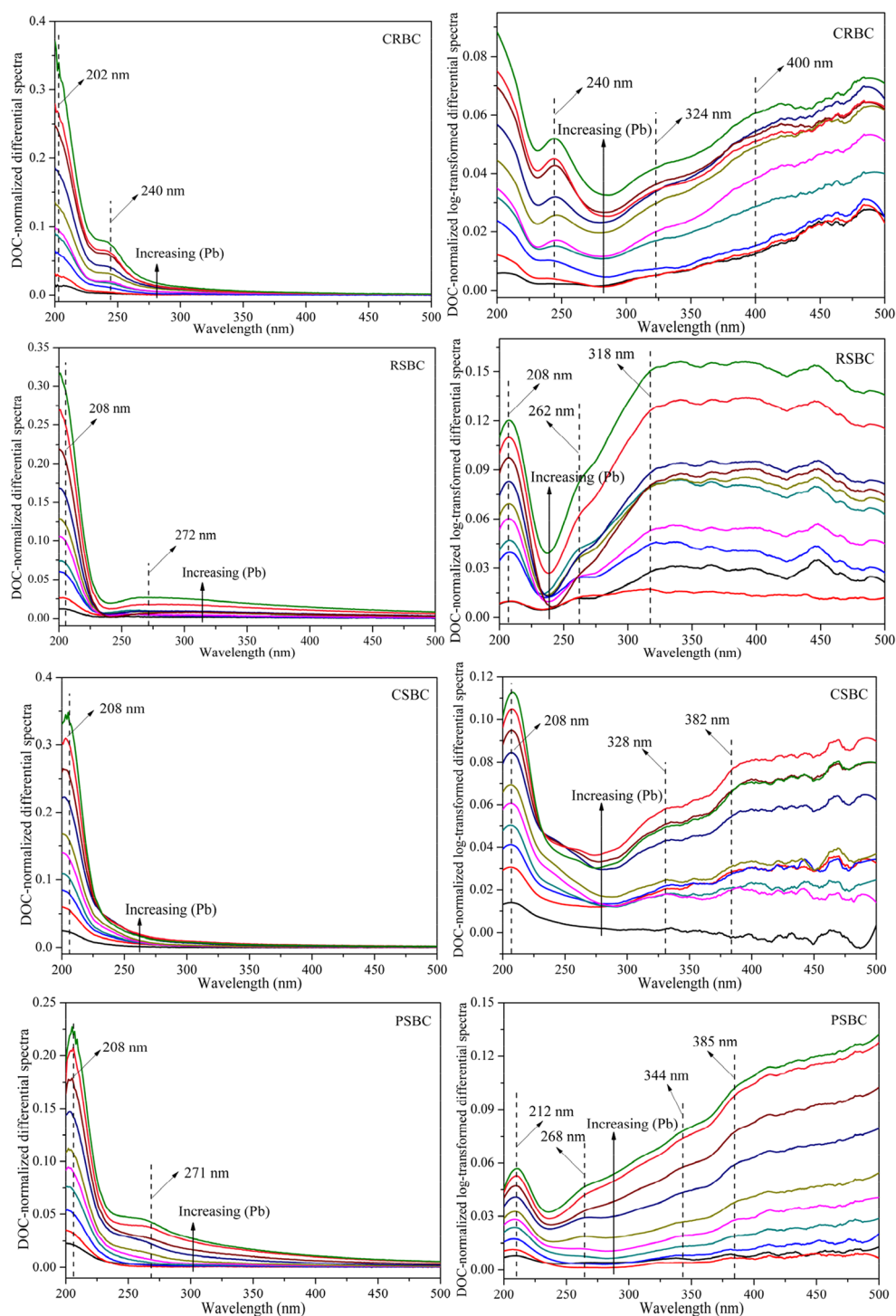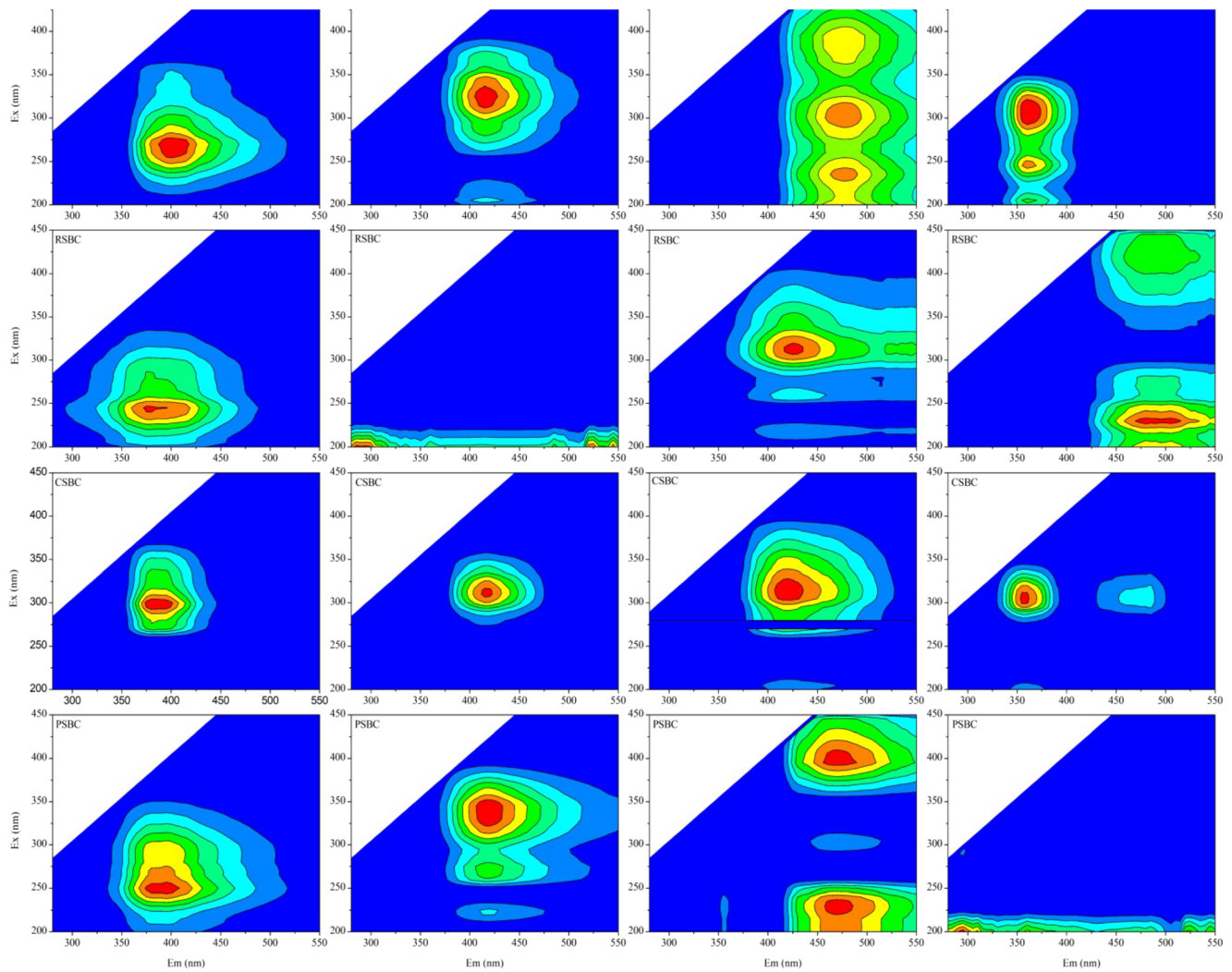

EEM-PARAFAC analysis

EEMs spectra can readily gather and reveal basic information about the fluorescent characteristics of DOM. However, the apparent overlapping of peaks in the primitive EEMs spectroscopy generally impedes the quantitative comprehension of DOM components (Li et al. 2017a; Sun et al. 2016). PARAFAC analysis can resolve the complex fluorescence

EEMs spectroscopy into several individual fluorescent fractions and decrease the interference caused by overlapping fluorophores among fluorescent compounds (Wu et al. 2012); thus, EEMs-PARAFAC became the most frequent method used for specific fluorescence information of DOM and interaction analysis of heavy metals with DOM.

EEM-PARAFAC analysis was used to study the fluorescent components of BDOMs in this study. As can be seen in

Fig. 2 Four fluorescence components (C1, C2, C3, and C4) derived from CRBC, RSBC, CSBC, and PSBC identified by EEM-PARAFAC analysis

Fig. 2, four individual fractions were identified in each biochars. In accordance with the previous reports of Park and Snyder (2018) and Chen et al. (2003), etc., the characteristics of the components were presented in Table 1. Spectral loadings of split-half validation results of the components and sum of squared error of the different numbers of PARAFAC components for determining the component numbers were shown in Fig. S5 and Fig. S6, respectively, which illustrated that four components were suitable for the PARAFAC analysis.

PARAFAC analysis can further provide the quantitative information regarding the distribution of each individual fluorescent fraction in BDOM samples. As for CRDOM, component C1 (Fmax = 451) had the richest abundant constituent, followed by component C2 (Fmax = 263), C4 (Fmax = 120), and C3 (Fmax = 99). For the RSDOM, component C1 (Fmax) was the dominant fraction, followed by components C3 (Fmax = 91) and C2 (Fmax = 64), whereas the Fmax value of component C4 (Fmax = 57) was the lowest. For CSDOM, the highest level of four components was C1 (Fmax = 134),

and the contents of C4 (Fmax = 74) were evidently lower than C1, C3 (Fmax = 93), and C2 (Fmax = 83). However, For PSDOM, C1 (Fmax = 344) had the highest level, followed by C2 (Fmax = 192), C3 (Fmax = 39), and C4 (Fmax = 11). These results implied that the fluorescent components and intensities were distinctively different among various BDOMs, and the fulvic-like and humic-like substances were the main fluorescent fractions of BDOMs.

Behavior of PARAFAC-derived components with addition of Pb(II) and Cu(II)

Fluorescence quenching curves of PARAFAC-derived components

Figure 3 displayed representation fluorescent quenching curves of every fraction with the increase of Pb(II) and Cu(II) concentrations. It can be seen that the quenching curves presented a large distinction between BDOM sources as well

Fig. 3 Changes in fluorescent intensity of the PARAFAC-derived components with increasing Pb(II) and Cu(II) addition
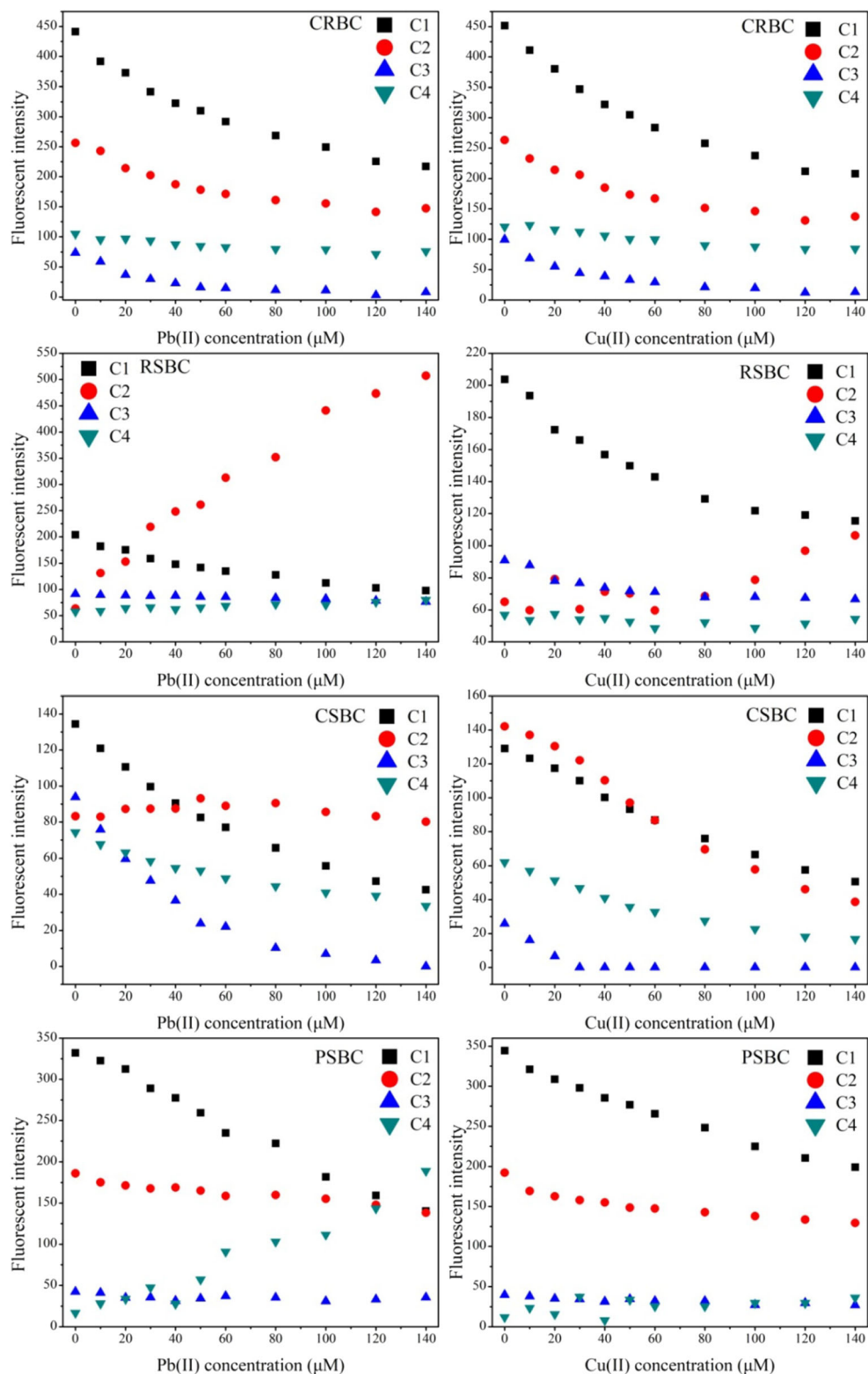
as metal kinds. The quenching properties of these fractions with the increase of Pb(II) and Cu(II) concentrations were extremely similar with those of sediment DOMs (Xu et al. 2019), hyperthermophilic compost-derived DOMs (Tang et al. 2019a, b), rice straw DOMs (Huang et al. 2018a), and leachate DOMs (Wu et al. 2011). Further an analysis showed that the gradual increase of Pb(II) and Cu(II) concentrations lead to similar quenching effects and the effects was distinct for CRDOM, illustrating that BDOM played an important role in the binding of Pb (II) and Cu(II). For RSDOM, component

C1 and C3 were quenched obviously by the two heavy metals, component C4 was in fluctuation, protein-like component C2 was enhanced by addition of Pb(II) and Cu(II). For CSDOM, a greater quenching effect was observed for Cu(II) than Pb(II) except that component C4 has hardly changed for Pb(II). For PSDOM, protein-like and fulvic-like component C4 has the same results as component C2 of RSDOM; the other components were quenched by the two heavy metals except component C3 was fluctuating by addition of Pb(II). These results strongly indicated that fulvic-like and humic-like substance played an important role in the complexation of heavy metals with BDOMs. However, the total protein-like fractions were enhanced by addition of Pb(II) and Cu(II). In order to study the changes in fluorescence intensity of different peaks at the same component, we analyzed the fluorescence intensity changes of different peaks as shown in Fig. S7. The fluorescence intensity changes of all the related fluorescent peaks in one PARAFAC component is consistent with that the change of Fmax. So in this study, Fmax could represent the complexation of each component with heavy metals during the quenching titration.

As is known to all, the fluorescence intensity of protein-like fractions were quenched or enhanced by addition of Pb(II) and Cu(II) ions. Thus, this method has seldom been employed to represent the complexation potential between protein-like fractions and heavy metals. In this work, the fluorescent intensity of the protein-like fraction was enhanced by addition of heavy metals. For Pb(II), fluorescence intensity has been increased at the initial stage, which could be owing to the addition of Pb(II) ions in the BDOM that stimulated some BDOM fluorophores (Huang et al. 2019; Yuan et al. 2015), while for Cu(II), the fluorescence intensity slightly decreased at the initial stage, but increased at later stage. The reasons were given by Yamashita and Jaffé (2008). Firstly, variations in quantum yields of protein fluorescent intensity by three-dimensional structure change of protein molecules may have occurred due to high concentrations of Pb(II) and Cu(II). Secondly, the fluorescence of protein-like substances may be quenched due to complexations with inorganic or other organic materials. Thus, the fluorescent intensity of such quenched protein-like fractions might be enhanced through the replacement of the primitive quencher with Pb(II) and Cu(II).

### Binding parameters of humic-like and fulvic-like substances

The quenching constant ($\log K_M$) computed using the Stern-Volmer equation for interaction between BDOMs and Pb(II)/Cu(II) were exhibited in Table S2. The values of $\log K_M$ ranged from 3.110 to 4.782 and 3.535 to 5.110 for Pb(II) and Cu(II), respectively. The result was similar with the ranges as those reported for Pb(II) and Cu(II) in compost-derived DOMs (Huang et al. 2018a; Guo et al. 2019; Tang et al. 2019a, b), landfill leachate-derived DOMs (Wu et al. 2012; Wu et al. 2011), macrophyte decomposition-derived DOMs (Yuan et al. 2015), and lake sediment-derived DOMs (Xu et al. 2019; Xu et al. 2013). The values of $\log K_M$ of the biochar samples or PARAFAC-derived components had no systematic trend. The fluorescence quenching curves of humic-like components C1, C2, and C3 for CRBC displayed an obvious declined trend with Pb(II)/Cu(II) addition, while the fulvic-like component C4 showed no clear changes. For RSDOM, the $\log K_M$ values of fulvic-like component C1 with Pb(II) and Cu(II) were 3.904 and 3.822, the $\log K_M$ values of C3 with Pb(II) and Cu(II) were 3.110 and 3.523, and component C4 with Pb(II) and Cu(II) failed to be modeled. For CSDOM, the binding constant of four components with Cu ranged from 3.991 to 5.110, the quenching constant of components with Pb(II) ranged from 3.916 to 4.693 excepting C2 failed to be modeled. As for PSDOM, the quenching constant of component C3 with Cu(II) can be modeled, while it was failed for Pb(II) to be modeled. The binding capability of BDOM with metals may be relied heavily on the chemical structure, aromaticity and the existence of a large number of aromatic acidic functional groups of BDOM (Li et al. 2017b). According to a previous study (Yuan et al. 2015), carboxyl and phenolic hydroxyl groups were mainly binding sites for DOM. The report of (Ohno et al. 2008) showed that DOM acidic contents and aromaticity were significant factors whose impact can be enhanced by binding with other pollutants. These observations distinctly indicated that combination of EEMs quenching titration and PARAFAC analysis could provide a deeper understanding for the binding characteristics of individual components within DOM.

Metal binding characterized by the 2D-UV-COS

In this work, 2D-COS was applied to study the binding dynamics of BDOM samples in response to Pb(II)/Cu(II) ions addition. The synchronous and asynchronous 2D-COS spectroscopy for the UV absorbance spectrum of complexation between BDOMs and Pb(II)/Cu(II) were exhibited in Fig. 4 and Fig. S8. At synchronous maps, only one positive auto-peak (200 nm) for the BDOMs-Pb(II)/Cu(II) complexation was found. For the BDOMs-Pb(II), the order of the intensity of the auto-peak: CRBC (Corr. = 0.197) > CSBC (Corr. = 0.183) > PSBC (Corr. = 0.110) > RSBC (Corr. = 0.105), and CSBC (Corr. = 0.031) > CRBC = RSBC (Corr. = 0.026) > PSBC (Corr. = 0.025) for BDOMs-Cu(II), illustrated that the spectral region of shorter wavelength was more sensitive than the spectral region of longer wavelength (Chen et al. 2015). However, the intensity in the BDOMs-Cu(II) was obviously decreased about 75.2–86.8% as compared with the BDOMs-Pb(II). The result was similar with the previous researches (Guo et al. 2017; Guo et al. 2019). There were no cross-

Fig. 4 2D-COS maps obtained from the UV-vis spectra of DOM-Pb in the CRBC (**a, b**), RSBC (**c, d**), CSBC (**e, f**), and PSBC (**g, h**). Red represents positive correlation and blue represents a negative correlation; a higher color intensity indicates a stronger positive or negative correlation
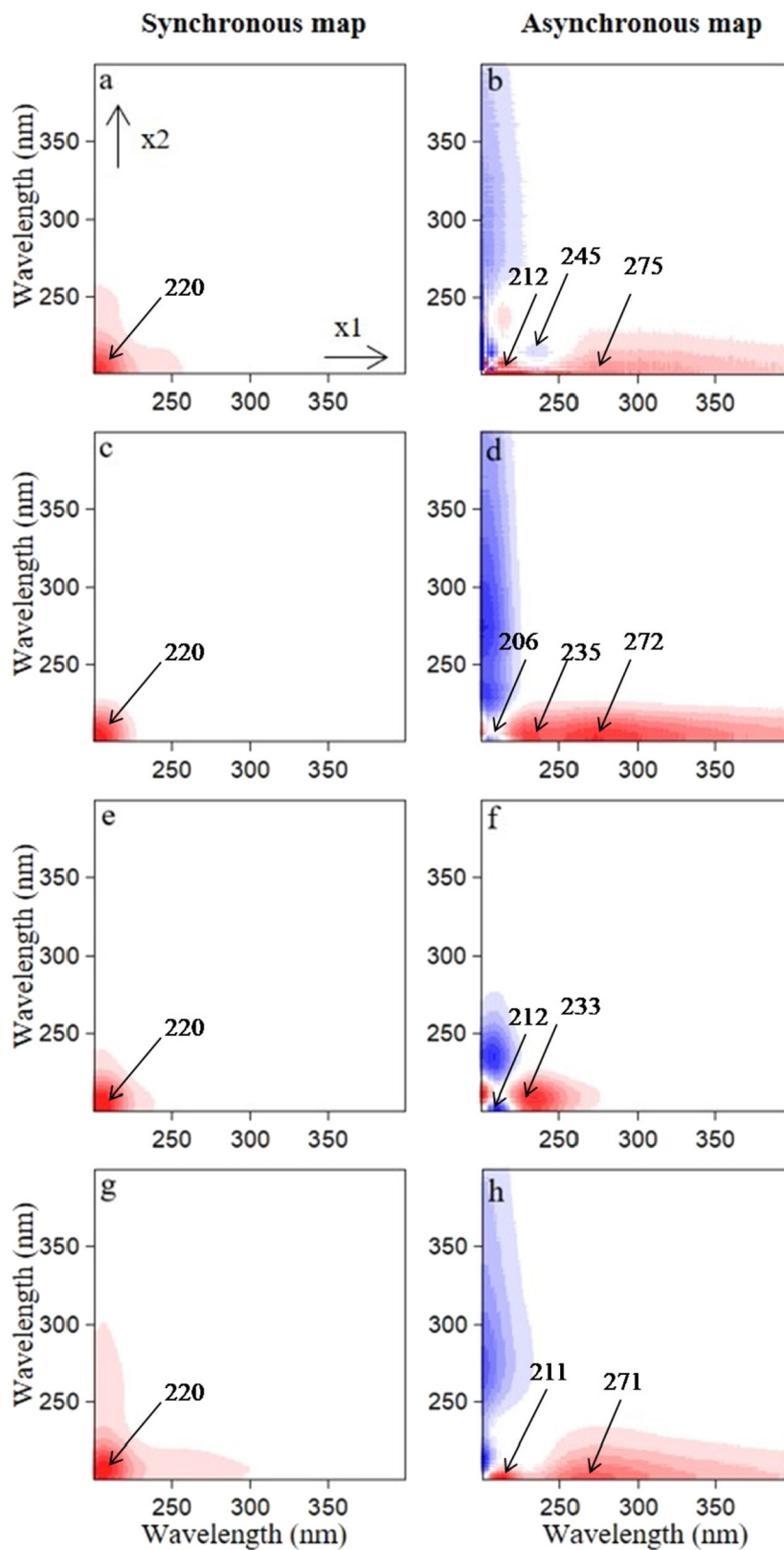
peaks at the synchronous spectra, indicating that the intensity varied at the same orientation for the corresponding spectra coordinates.

The asynchronous map has no auto-peaks, and consists of cross-peaks located at off-diagonal positions. (Guo et al. 2019). In the asynchronous spectrum, the detailed position

of spectra and the relationship of the signs and the binding sequence (according to the consequence of Noda's rule) were presented at Table S3. The result suggested the binding of BDOMs with Pb(II)/Cu(II) occurred at a shorter wavelength, and also suggested the differences in the heterogeneous distribution and binding affinities between BDOM-Pb(II) and BDOM-Cu(II).

Similar to the differential absorption spectra, 2D-UV-COS can also be employed to identify the overlapping absorption peaks of low intensity (Chen et al. 2019; Chen et al. 2015) The results were basically consistent with those of the differential spectrum analysis. The variations of the absorbance with the metal addition were verified by the 2D-COS as exhibited in Fig. S9. The concentrations of both Pb(II) and Cu(II) were obviously associated with the absorbance in four BDOM samples. The absorbance values exhibited an obvious positive correlation with the Pb(II)/Cu(II) addition.

Metal binding characterized by the 2D-SF-COS

As shown in the Fig. S10, an obvious decrease of BDOMs fluorescence intensity, a slight change in shape, and a slight blue shift were observed in SF spectra with the addition of Pb(II) and Cu(II) ions. These findings indicated that there was obvious interaction between BDOMs and Pb(II)/Cu(II) and addition of Pb(II)/Cu(II) could result in molecular conformation changes of BDOMs (Zhao et al. 2019). To further investigate the binding characteristics, the 2D-COS spectrum generated from the SF of BDOM-Pb(II) and Cu(II) were exhibited in Fig. 5 and Fig. S11. One predominant auto-peak centered at 341 nm in synchronous 2D-COS maps of the CRBC and PSBC samples, and one positive auto-peak was found at 328 nm along the diagonal line of the synchronous maps for CSBC sample. These results indicated that the interaction of DOM-Pb(II)/Cu(II) samples was associated with fulvic-like substances (Xu et al. 2018). The synchronous showed two auto-peaks at 311, 370 nm, one positive and three negative cross-peaks at the ×1 wavelength of 371, 312, 370, and 468 nm for RSDOM-Pb(II), and only one positive peak (318 nm) for RSDOM-Cu(II). The interaction of the RSDOM with Pb(II) was associated with fulvic-like substances at ×1 wavelength of 371, 312, and 370 nm, and humic-like substances at ×1 wavelength of 468 nm, while only fulvic-like substances for RSDOM-Cu(II). According to the results obtained above, the fulvic-like substance was more susceptible to change in the concentrations of Pb(II) and Cu(II) ions. The order of sensitivity can be sequenced as follows for Pb(II): CRBC (Corr. = 44,533,327) → CSBC (Corr. = 21,470,799) → PSBC (Corr. = 10,522,282) → RSBC (Corr. = 51,734), and CRBC (Corr. = 27,254,547) → CSBC (Corr. = 4,789,802) → PSBC (Corr. = 2,393,269) → RSBC (Corr. = 12,183) for Cu(II) at ×1 according to the synchronous maps, suggesting that the RSDOM displayed a

lower sensibility as compared with that of CRDOM, CSDOM, and PSDOM due to the increase of Pb(II)/Cu(II) ions concentration (Guo et al. 2019). However, the intensity in the BDOM-Cu(II) was obviously decreased about 38.8% for CRBC and about 75% for others as compared with the BDOM-Pb(II). The result was consistent with the result obtained from the 2D-UV-COS analysis. This may be attributed to the paramagnetism and radius of heavy metals. More specifically, the different electron shells distribution in diverse metal ions and the different electron pairs ability make the difference in affinity of metal ions to the same organic ligands (Huang et al. 2018a; Irving and Williams 1948).

In the asynchronous maps, the detailed position of cross-peaks, the relationship of the signs, and the binding sequence were showed in Table S4. Changes in the intensity with the metal addition identified by the 2D-SF-COS were presented in Fig. S12. We can see from that the fulvic-like substances had a higher affinity for Pb(II) and Cu(II) than humic-like substances, which was similar to the researches of Xu et al. (2019) and Chen et al. (2015). In contrast, some reports obtained the opinion that the protein-like substance had a stronger affinity than the fulvic-like and humic-like substance (Huang et al. 2019; Wu et al. 2011; Wu et al. 2012). These contradictory results are possibly related to the origins of DOM samples. DOMs derived from different sources have the differences in molecular weight, molecular structure, molecular conformation, and charge and steric hindrance, which make the different affinity for the same metals. (Li et al. 2017a; Philippe and Schaumann 2014).

## Metal binding characterized by the 2D-FTIR-COS

Compared to UV and SF two-dimensional spectroscopy, FTIR can obtain the presence information of specific functional groups (Yan et al. 2016; Xu et al. 2018). Figure S13 and Fig. S14 exhibited the FTIR absorbance spectra of BDOM-Pb and BDOM-Cu, respectively. The synchronous and asynchronous spectrum of BDOM binding with Pb(II) from 1800 to 900 cm^{-1} were presented in Fig. 6. The synchronous maps exhibited four auto-peaks at 1594, 1384, 1153, and 991 cm^{-1} in CRDOM; five auto-peaks at 1783, 1552, 1384, 1111, and 910 cm^{-1} in RSDOM; four auto-peaks at 1581, 1384, 1058, and 977 cm^{-1} in CSDOM; and four auto-peaks at 1650, 1390, 1272, and 1132 cm^{-1} in PSBC-derived DOM. In the synchronous maps, as can be seen, the signs of the auto or cross-peaks were all positive, except for ones located at 1051 and 970 cm^{-1} in CRDOM. The result suggested that the signals of the functional groups underwent the same direction because of the addition of Pb(II) ions.

As for the asynchronous spectrum, negative and positive cross-peaks were all found. The detailed information about the positions and the assignments of the peaks and the relationships of the signs were shown in Table S5. The bands at

Fig. 5 2D-COS maps obtained from the SF spectra of DOM-Pb in the CRBC (**a**, **b**), RSBC (**c**, **d**), CSBC (**e**, **f**), and PSBC (**g**, **h**). Red represents positive correlation and blue represents a negative correlation; a higher color intensity indicates a stronger positive or negative correlation
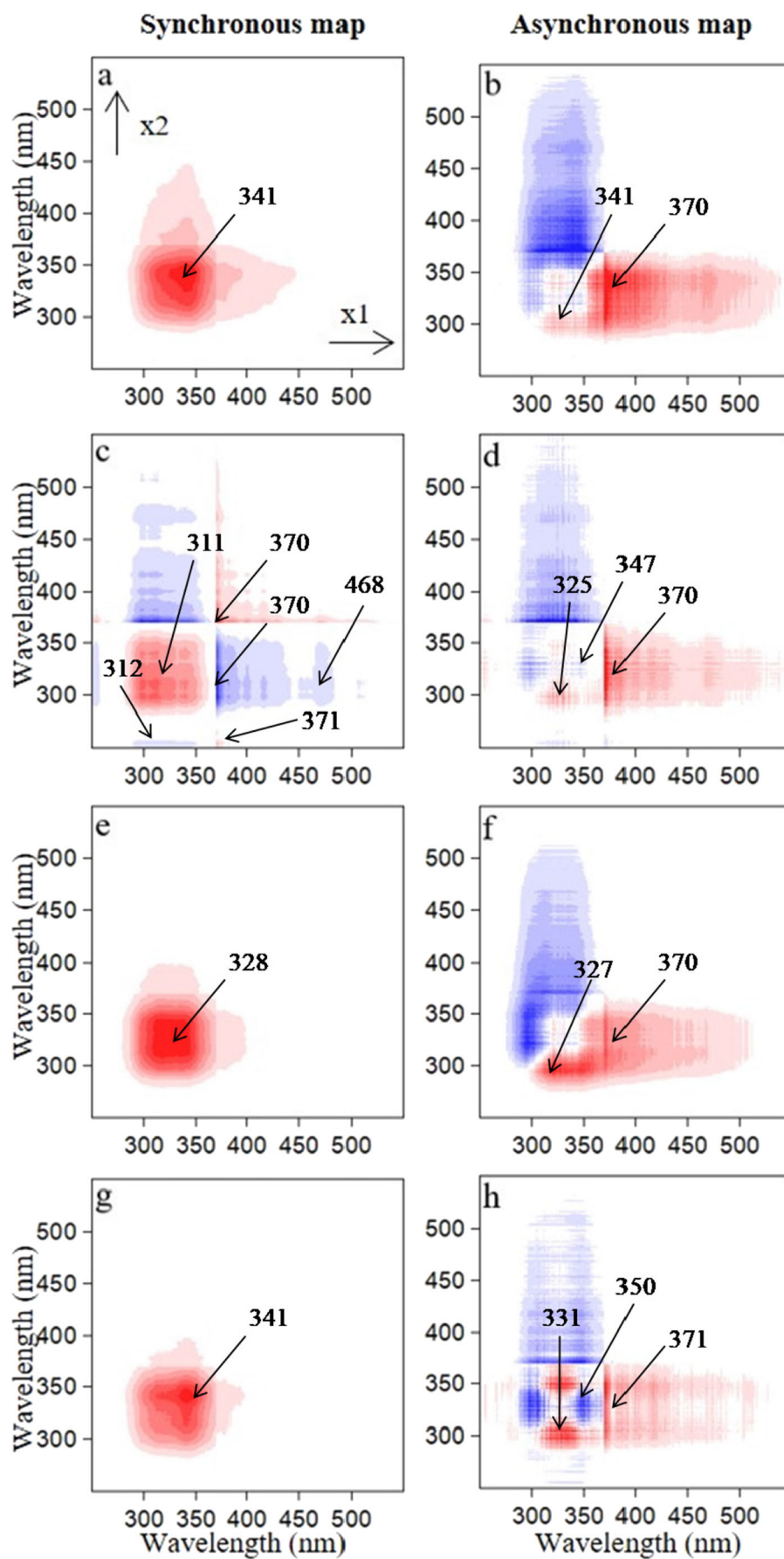
Fig. 6 2D-COS maps obtained from the FTIR spectra of DOM-Pb in the CRBC (**a, b**), RSBC (**c, d**), CSBC (**e, f**), and PSBC (**g, h**). Red represents positive correlation and blue represents a negative correlation; a higher color intensity indicates a stronger positive or negative correlation
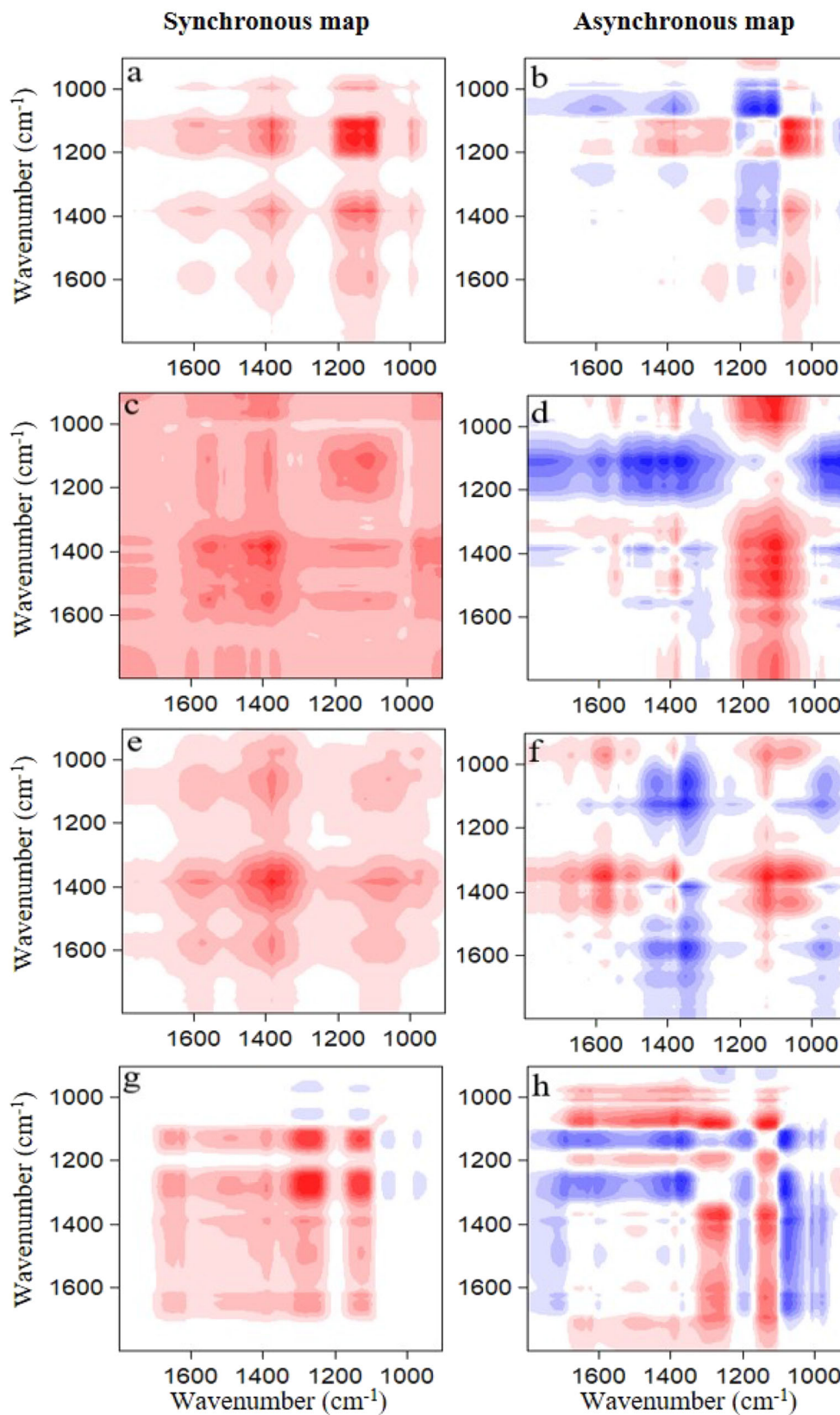
1650 cm^{-1} corresponded to the C=C stretching of aromatic (He et al. 2011). The peaks at 1581, 1538, 1504, 1427, 1419, 1272, and 1265 cm^{-1} belong to the C-O stretching (or OH deformation) and C=O stretching of carboxylic acid groups (Chen et al. 2015; He et al. 2011; He et al. 2014; Huang et al. 2018a; Li et al. 2011; Tang et al. 2019a, b). The bands at 1195,
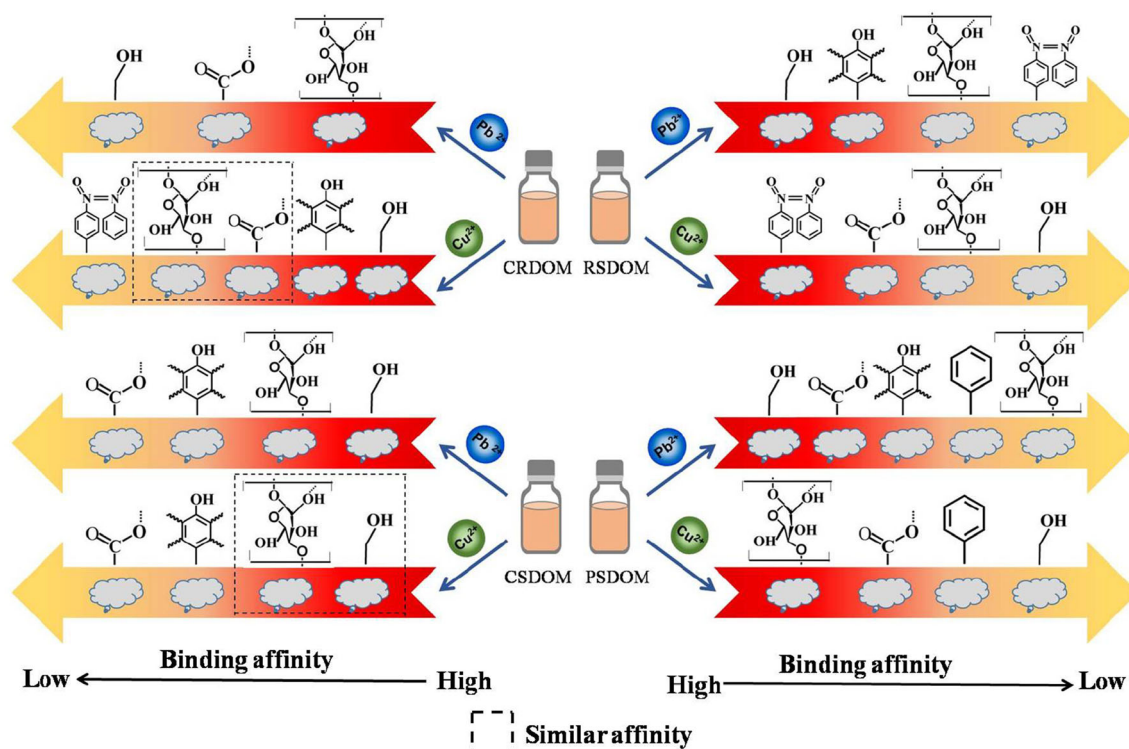
Fig. 7 Binding affinities of BDOMs to Pb(II) and Cu(II)

1184, 1141, 1135, 1124, 1107, 1103 cm^{-1} were attributable to the aliphatic C-OH stretching (He et al. 2014; Tang et al. 2019a, b; Li et al. 2011). The 1072, 1062, 985, and 977, 910 cm^{-1} signals can be ascribed to the C-O stretching of polysaccharides (He et al. 2011; Li et al. 2011; Tang et al. 2019a, b). The peaks at 1394 and 1384 cm^{-1} were assigned as the phenolic OH deformation (Huang et al. 2018a; Tang et al. 2019a, b; Guo et al. 2019). The peaks at 1471 cm^{-1} were attributable to N=O stretching of aromatic groups (Huang et al. 2019). The peaks at 1355 and 1351 cm^{-1} are ascribed to the aliphatic C-H deformation and C-OH stretching (Chen et al. 2015). In accordance with the sequential order rules (Noda and Ozaki 2004), the changes of functional groups in the binding procedure of CRDOM with Pb(II) were in the sequence of polysaccharides→carboxyl→aliphatic groups, the binding process in RSBC could be proposed as follows: aliphatic groups→phenolic groups→polysaccharides→the N=O stretching of aromatic groups, the binding sequence in CSBC was as follows: aliphatic groups→polysaccharides→phenolic groups→carboxyl, and the binding sequence of functional groups changes in PSBC was as followed: aliphatic groups→carboxyl→phenolic groups→C=C stretching of aromatic→polysaccharides. It could be concluded that polysaccharides in RSDOM provided the fastest response to Pb(II) addition, while aliphatic groups in RSDOM, CSDOM, and PSDOM gave the most sensitive group to Pb(II) addition. These results verified the presence of the heterogeneity of the binding properties between BDOM fractions and heavy

metals and a relative discrepancy in the binding process of different BDOMs.

The spectrum of 2D-FTIR-COS of BDOM-Cu(II) were presented in Fig. S15. It could be seen that the results of the synchronous spectrums were extremely similar with the characteristics of BDOM-Pb(II), which indicated a similar binding process of BDOMs with Pb(II) and Cu(II). However, differences were found for the sensibility and complexing order of the functional groups of the corresponding spectra regions. The detailed information about the signs and positions of cross-peaks and the assignments of spectra and the relationships of these signs were exhibited at Table S6.

According to the Noda's rule (Noda and Ozaki 2004), the complexing orders of functional groups of CRDOM to Cu(II) were aliphatic groups→phenolic groups→carboxyl and polysaccharides→N=O stretching of aromatic groups, the bounding sequence of RSDOM to Cu(II) was the N=O stretching of aromatic groups→carboxyl→polysaccharides→aliphatic groups, the bounding sequence of CSDOM to Cu(II) was aliphatic groups and polysaccharides→phenolic groups→carboxyl, and the bounding sequence of PSDOM to Cu(II) was polysaccharides→carboxylic→C=C stretching of aromatic→aliphatic groups.

The results of 2D-FTIR-COS suggested that not only the fluorescent groups, but also some non-fluorescent groups (e.g., polysaccharides) of BDOMs, were related to the interaction process of Pb(II) and Cu(II) with BDOM. The difference of binding order between Pb(II)

Fig. 8 2D-COS maps obtained from the SF-FTIR heterospectral correlation spectra of DOM-Pb in the CRBC (**a, b**), RSBC (**c, d**), CSBC (**e, f**), and PSBC (**g, h**). Red represents positive correlation and blue represents a negative correlation; a higher color intensity indicates a stronger positive or negative correlation
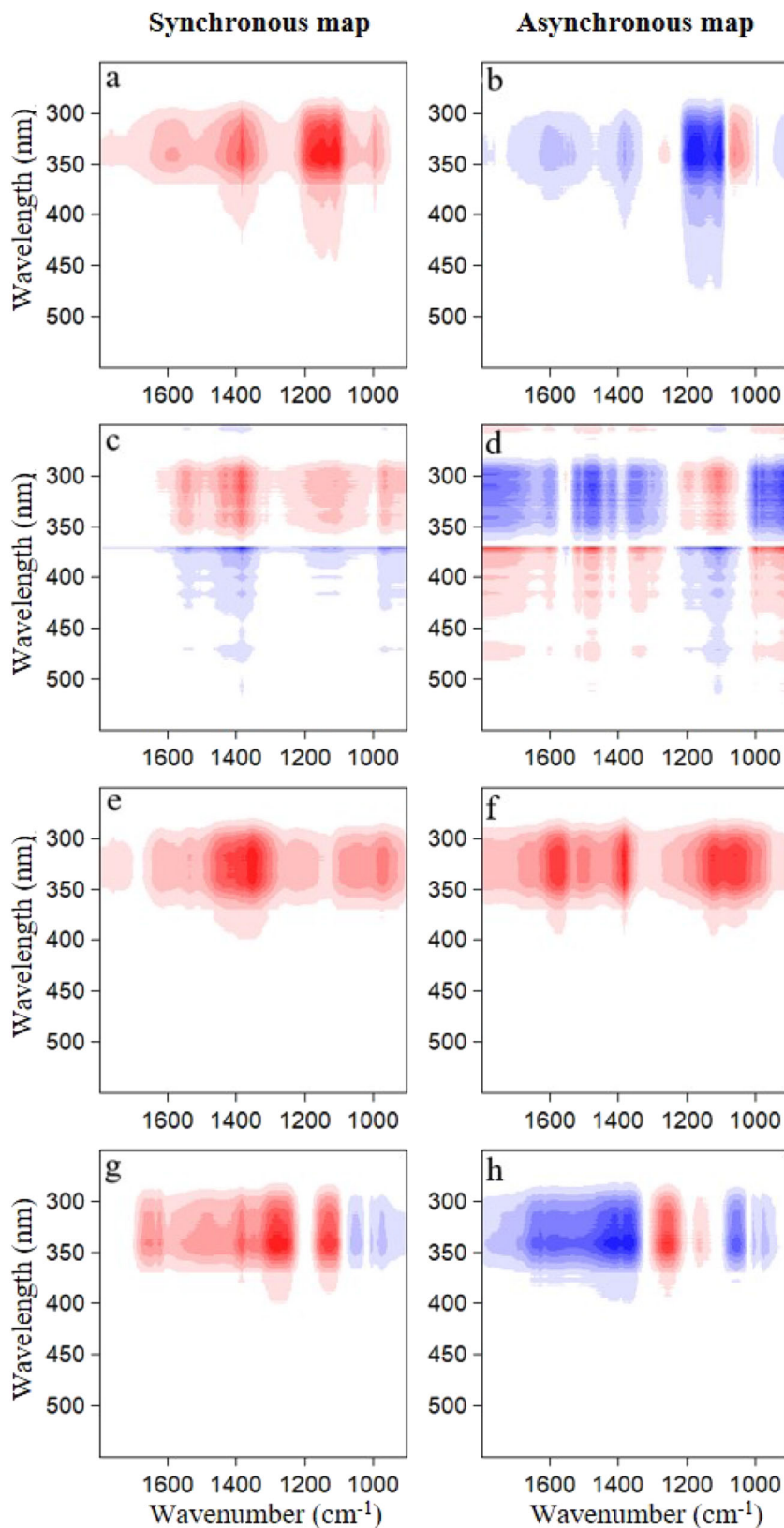
and Cu(II) may be related to the special chemical characteristics of them (Huang et al. 2019; Li et al. 2017a), but the more precise reasons still need further study. In order to make the binding procedure of BDOMs with Pb(II) and Cu(II) clearer, a detailed image based on the changes of BDOM molecule level was drawn (Fig. 7).

2D SF/FTIR heterospectral COS analysis

This study applied a 2D heterospectral COS analysis of SF/FTIR to research the bands assignments and the correspondence between two supplementary techniques of SF and FTIR (Chen et al. 2015). The heterospectral 2D-COS spectra could act as a visual assistance to help depict the structural changes of BDOM during the Pb(II) and Cu(II) binding (Chen et al. 2019). The synchronous and asynchronous spectra of the hetero-2DCOS of BDOM-Pb(II) were presented in Fig. 8. At the synchronous maps, for CRDOM, five negative cross-peaks were found in the FTIR positions of 1587, 1380, 1157, and 1107 cm^{-1} and the corresponding fluorescent region of 290–410 nm. For RSDOM, five cross-peaks were located in the FTIR regions of 1584, 1432, 1384, 1111, and 968 cm^{-1}, the signs were positive at the fluorescent region of 285–355 nm, and the signs were negative at the fluorescent region of 370–450 nm. Four positive cross-peaks were found in the FTIR regions of 1766, 1538, 1355, and 970 cm^{-1} and the corresponding fluorescent regions of 318 and 324 nm for CSDOM in the synchronous map. For PSDOM, four positive and two negative cross-peaks were located in the FTIR positions of 1656, 1384, 1282, 1132, 1051, and 970 cm^{-1} and the correspondence fluorescent region of 341 nm. In the asynchronous spectrum, the locations of the cross-peaks were similar with the synchronous map. Some of them were divided into different parts and the signs have been changed. For CRDOM, functional groups at 1587, 1384, 1265, 1170, 1103, 1058, and 910 cm^{-1} were related to the fulvic-like substance (342 nm) (He et al. 2011). The groups at 1776, 1483, 1351, and 925 cm^{-1} were associated with the protein-like substance (285–300 nm), fulvic-like substance (300–355 and 370–380 nm), and humic-like substance (380–440 nm) for RSDOM. In the CSBC sample, the groups at 1581, 1510, 1384, 1124, and 1062 cm^{-1} were ascribed to the fulvic-like substance (318 nm) (Li et al. 2011). For PSDOM, the groups at 1637, 1598, 1415, 1373, 1255, 1162, 1051, and 970 cm^{-1} were related to fulvic substances (341 nm). These results suggested that the carboxylic, aliphatic, aromatic, and phenolic groups were the basic fluorescent units for fulvic-like and humic-like substances, which were consistent with the results of Tang et al. (2019a, b).

As mentioned in 2D-FTIR-COS, the sequential information about the variations of FTIR and SF spectrum were provided in the asynchronous maps of hetero spectral. For CRDOM, at the fluorescent region of 342 nm, there were two positive signs at 1265 and 1058 cm^{-1}, and five negative signs at 1587, 1384, 1170, 1103, and 910 cm^{-1}, indicating that the spectra changes of carboxylic, phenolic, and aliphatic groups were found before the fluorescent changes of fulvic-like substances. One positive (1111 cm^{-1}) and five negative (1776, 1483, 1351, and 925 cm^{-1}) signs were found at 295, 311, and 341 nm in RSDOM, suggesting that the changes of

aliphatic groups occurred before the fluorescent changes of the protein-like and fulvic-like substance, while aromatic and carboxylic groups occurred after the fluorescent changes of the protein-like and fulvic-like substance. The opposite signs were observed at 370, 398, 416, and 471 nm, which suggested that fluorescent response of the fulvic-like and humic-like substance occurred before the spectra changes of aliphatic, aromatic, and carboxylic. All of six positive signs (1581, 1510, 1384, 1124, and 1062 cm^{-1}) were observed at 318 nm in CSDOM, which indicated that the fluorescent changes of the fulvic-like substance were observed before the FTIR spectra changes of aliphatic, phenolic, and carboxylic groups. For PSDOM, the fluorescent intensity of the fulvic-like substance changed before the FTIR spectra of aliphatic, carboxylic, phenolic, and aromatic groups (Xu et al. 2019).

Compared to BDOM-Pb(II), the synchronous and asynchronous spectrum of the hetero-2DCOS of BDOM-Cu(II) almost have the same peak position except RSDOM, but the signs of positive or negative and the intensity were different (Fig. S16,). For CRDOM, the result that the spectra changes of aliphatic, aromatic and carboxylic groups were observed before the fluorescent changes of the fulvic-like substance was similar with DOM-Pb(II). The different result found in RSDOM and DOM-Cu(II) only had peaks at 285–360 nm in synchronous and asynchronous maps, and the spectra intensity changes of aromatic, carboxylic, and aliphatic groups occurred before the fluorescent changes of fulvic-like substance. The result of CSDOM-Cu(II) was the same as the DOM-Pb(II) in synchronous and asynchronous maps, in which the fluorescent change of the fulvic-like substance were observed before the FTIR spectra changes of aliphatic, phenolic, and carboxylic groups. For PSDOM, the result of DOM-Cu(II) was similar with the DOM-Pb(II), in which the fluorescent intensity of the fulvic-like substance changed before the FTIR spectra of aliphatic, aromatic, and aliphatic.

Conclusion

EEM-PARAFAC, DAS, and 2D-COS analysis were used to probe the composition of BDOM and the binding process and mechanisms between BDOM and Pb(II), Cu(II). The main components of fulvic-like and humic-like substances were obtained by using the EEM-PARAFAC method from BDOM. Although the original UV-vis absorption spectra was featureless, DAS performed an uneven distribution of functional groups and active sites within the BDOM pool for Pb(II) and Cu(II) binding, and also indicated the binding heterogeneities of different chromophoric and fluorescent groups. 2D-COS analyses of UV-vis, SF, and FTIR provided the binding order and binding characteristics originated in changes in the concentration of Pb(II) and Cu(II) over 2D-

COS maps, and revealed the heterogeneities of binding sites within BDOM-Pb(II) and Cu(II). The result of this work provided a further comprehension for the difference in binding characteristics resulted by different BDOMs and provided guidance for understanding the mobility and transformation of heavy metals in the biochar repairing soil or water.

Authors' contributions All authors contributed to the study conception and design. Material preparation, data collection, and analysis were performed by Xiaoli Zhang, Xuewei Cai, Zhaowei Wang, Xing Yang, Shan Li, Guiwei Liang, and Xiaoyun Xie. The first draft of the manuscript was written by Xiaoli Zhang and all authors commented on previous versions of the manuscript. All authors read and approved the final manuscript.

Data availability All the data and tools/models used for this work are publicly available.

Compliance with ethical standards

Conflict of interest The authors declare that they have no conflict of interest.

Ethics approval and consent to participate Not applicable.

Consent for publication Not applicable.

References

Abel S, Peters A, Trinks S, Schonsky H, Facklam M, Wessolek G (2013) Impact of biochar and hydrochar addition on water retention and water repellency of sandy soil. Geoderma 202:183–191

Beesley L, Inneh OS, Norton G, Moreno-Jiménez E, Pardo T, Clemente R, Dawson JJC (2014) Assessing influence of compost and biochar amendment on the mobility and toxicity of metals and arsenic in a naturally contaminated mine soil. Environ Pollut 186:195–202

Chen W, Westerhoff P, Leenheer JA, Booksh K (2003) Fluorescence excitation-emission matrix regional integration to quantity spectra for dissolved organic matter. Environ Sci Technol 37:5701–5710

Chen W, Habibul N, Liu XY, Sheng GP, Yu HQ (2015) FTIR and synchronous fluorescence heterospectral two-dimensional correlation analyses on the binding characteristics of copper onto dissolved organic matter. Environ Sci Technol 49:2052–2058

Chen W, Teng CY, Qian C, Yu HQ (2019) Characterization properties and environmental behaviors of dissolved organic matter using two-dimensional correlation spectroscopy analysis. Environ Sci Technol 53:4683–4694

Eykelbosh AJ, Johnson MS, Couto EG (2015) Biochar decreases dissolved organic carbon but not nitrate leaching in relation to vinasse application in a Brazilian sugarcane soil. J Environ Manag 149:9–16

Feng WJ, Zhang SR, Zhong QM, Wang GY, Pan XM, Xu XX, Zhou W, Li T, Luo L, Zhang YZ (2020) Soil washing remediation of heavy metal from contaminated soil with EDTMP and PAA: properties, optimization, and risk assessment. J Hazard Mater 381:120997

Ferrie RP, Hewitt GE, Anderson BD (2017) A fluorescence quenching analysis of the binding of fluoroquinolones to humic acid. Appl Spectrosc 71:2512–2518

Gao Y, Yan MQ, Korshin GV (2015a) Effects of ionic strength on the chromophores of dissolved organic matter. Environ Sci Technol 49(10):5905–5912

Gao Y, Yan MQ, Korshin G (2015b) Effects of calcium chromophores of dissolved organic matter and their interaction with copper. Water Res 81:47–53

Gu YL, Yin MX, Zhang HM, Wang YQ, Shi JH (2015) Study on the binding interaction of chromium(VI) with humic acid using UV-vis, fluorescence spectroscopy and molecular modeling. Spectrochim. Acta A 136:1702–1709

Guo XJ, Li YZ, Feng YH, Yuan DH (2017) Using fluorescence quenching combined with two-dimensional correlation fluorescence spectroscopy to characterise the binding-site heterogeneity of dissolved organic matter with copper and mercury in lake sediments. Environ Chem 14:91–98

Guo XJ, He XS, Li CW, Li NX (2019) The binding properties of copper and lead onto compost-derived DOM using Fourier-transform infrared, UV-vis and fluorescence spectra combined with two-dimensional correlation analysis. J Hazard Mater 365:457–466

He XS, Xi BD, Wei ZM, Guo XJ, Li MX, An D, Liu HL (2011) Spectroscopic characterization of water extractable organic matter during composting of municipal solid waste. Chemosphere 82:541–548

He XS, Xi BD, Zhang ZY, Gao RT, Tan WB, Cui DY (2014) Insight into the evolution, redox, and metal binding properties of dissolved organic matter from municipal solid wastes using two-dimensional correlation spectroscopy. Chemosphere 711:701–707

Hu SH, Lu C, Zhang CJ, Zhang YJ, Yao HR, Wu YG (2016) Effects of fresh and degraded dissolved organic matter derived from maize straw on copper sorption farmland loess. J Soils Sediments 16:327–338

Huang M, Li ZW, Huang B, Luo NL, Zhang X, Zhai QQ, Zeng GM (2018a) Investigating binding characteristics of cadmium and copper to DOM derived from compost and rice straw using EEM-PARAFAC combined with two-dimensional FTIR correlation analysis. J Hazard Mater 344:539–548

Huang S, Gan WH, Yan MQ, Zhang XR, Zhong Y, Yang X (2018b) Differential UV-vis absorbance can characterize the reaction of organic matter with ClO₂. Water Res 139:442–449

Huang M, Li ZW, Luo NL, Yang R, Wen JJ, Huang B, Zeng GM (2019) Application potential of biochar in environment: insight from degradation of biochar-derived from DOM and complexation of DOM with heavy metals. Sci Total Environ 646:220–228

Hur J, Lee BM (2011) Characterization of binding site heterogeneity for copper within dissolved organic matter fractions using two-dimensional correlation fluorescence spectroscopy. Chemosphere 83:1603–1611

Irving DH, Williams RJP (1948) Order of stability of metal complexes. Nature 162:746–747

Jin Y, Liang XQ, He MM, Liu Y, Tian GM, Shi JY (2016) Manure biochar influence upon soil properties, phosphorus distribution and phosphatase activities: a microcosm incubation study. Chemosphere 142:128–135

Jin J, Sun K, Yang Y, Wang ZY, Han LF, Wang XK, Wu FC, Xing BS (2018) Comparison between soil- and biochar-derived humic acids: composition, conformation, and phenanthrene sorption. Environ Sci Technol 52:1880–1888

Karami N, Clemente R, Moreno-Jimenez E, Lepp NW, Beesley L (2011) Efficiency of green waste compost and biochar soil amendments for reducing lead and copper mobility and uptake to ryegrass. J Hazard Mater 191:41–48

Kim HJ, Kim SB, Kim JK (2006) Two-dimensional heterospectral correlation analysis of wide-angle X-ray scattering and infrared spectroscopy for specific chemical interactions in weakly interacting block copolymers. J Phys Chem B 110:23123–23129

Lawaetz AJ, Stedmon CA (2009) Fluorescent intensity calibration using the raman scatter peak of water. Appl Spectrosc 63:936–940

Li XW, Xing MY, Yang J, Huang ZD (2011) Compositional and functional features of humic acid-like fractions from vermicomposting of sewage sludge and cow dung. J Hazard Mater 185:740–748

Li M, Zhang AF, Wu HM, Liu H, Lv JL (2017a) Predicting potential release of dissolved organic matter from biochars derived from agricultural residues using fluorescence and ultraviolet absorbance. J Hazard Mater 334:86–92

Li WW, Zhang FF, Ye Q, Wu D, Wang LY, Yu YH, Deng B, Du JZ (2017b) Composition and copper binding properties of aquatic fulvic acids in eutrophic Taihu Lake, China. Chemosphere 172:496–504

Li G, Khan S, Ibrahim M, Sun TR, Tang JF, Cotner JB, Xu YY (2018) Biochars induced modification of dissolved organic matter (DOM) in soil and its impact on mobility and bioaccumulation of arsenic and cadmium. J Hazard Mater 348:100–108

Liu HK, Xu F, Xie YL, Wang K, Zhang AK, Li LL, Xu H (2018) Effect of modified coconut shell biochar on availability of heavy metals and biochemical characteristics of soil in multiple heavy metals contaminated soil. Sci Total Environ 645:702–709

Liu CH, Chu WY, Li H, Boyd SA, Teppen BJ, Mao JD, Lehmann JL, Zhang W (2019) Quantification and characterization of dissolved organic carbon from biochars. Geoderma 335:161–169

Lu YJ, Yan MQ, Korshin GV (2017) Spectrascopic study of interactions of lead(II) ions with dissolved organic matter: evidence of preferential engagement of carboxylic groups. Geochim Cosmochim Acta 213:308–316

Mohan D, Sarswat A, Ok YS, Pittman JCU (2014) Organic and inorganic contaminants removal from water with biochar, a renewable, low cost and sustainable absorbent—a critical review. Bioresour Technol 160:191–202

Noda I, Ozaki Y (2004) Two-dimensional correlation spectroscopy-applications in vibrational and optical spectroscopy. Wiley, London

Ohno T, Amirbahman A, Bro R (2008) Parallel factor analysis of excitation-emission matrix fluorescence spectra of water soluble soil organic matter as basis for the determination of conditional metal binding parameters. Environ Sci Technol 42:186–192

Ozaki Y, Czarnik-Matusewicz B, Šašic S (2001) Two-dimensional correlation spectroscopy in analytical chemistry. Anal Sci 17:i663–i666

Park M, Snyder SA (2018) Sample handling and data processing for fluorescent excitation-emission matrix (EEM) of dissolved organic matter (DOM). Chemosphere 193:530–537

Philippe A, Schaumann GE (2014) Interactions of dissolved organic matter with natural and engineered inorganic colloids: a review. Environ Sci Technol 48:8946–8962

Soja G, Wimmer B, Rosner F, Faber F, Dersch G, Chamier J, Pardeller G, Ameur D, Keiblinger K, Zehetner F (2017) Compost and biochar interaction with copper immobilisation in copper-enriched vineyard soils. Appl Geochem 88:40–48

Sun J, Guo L, Li QQ, Zhao YG, Gao MC, She ZL, Wang GS (2016) Structure and functional properties of organic matters in extracellular polymeric substances (EPS) and dissolved organic matters (DOM) after heat pretreatment with waste sludge. Bioresour Technol 219:614–623

Tang JF, Li XH, Luo Y, Li G, Khan S (2016) Spectroscopic characterization of dissolved organic matter derived from different biochars and their polycylic aromatic hydrocarbons (PAHs) binding affinities. Chemosphere 152:399–406

Tang JY, Zhang JC, Ren LH, Zhou YY, Gao J, Luo L, Yang J, Peng QH, Huang HL, Chen AW (2019a) Diagnosis of soil contamination using microbiological indices: a review on heavy metal pollution. J Environ Manag 242:121–130

Tang J, Zhuang L, Yu Z, Liu XM, Wang YQ, Wen P, Zhou SG (2019b) Insight into complexation of cu(II) to hyperthermophilic compost-derived humic acids by EEM-PARAFAC combined with heterospectral two dimensional correlation analyses. Sci Total Environ 656:29–38

Wang Y, Zhang D, Shen Z, Feng C, Chen J (2013) Revealing sources and distribution changes of dissolved organic matter (DOM) in pore water of sediment from the Yangtze estuary. PLoS One 8(10):e76633

Wu J, Zhang H, He PJ, Shao LM (2011) Insight into the heavy metal binding potential of dissolved organic matter in WSW leachate using EEM quenching combined with PARAFAC analysis. Water Res 45:1711–1719

Wu J, Zhang H, Yao QS, Shao LM, He PJ (2012) Toward understanding the role of individual fluorescent components in DOM-metal binding. J Hazard Mater 215-216:294–301

Xiao YH, Sara-Aho T, Hartikainen H, Vähätalo AV (2013) Contribution of ferric iron to light absorption by chromophoric dissolved organic matter. Limnol Oceanogr 58(2):653–662

Xiao X, Xi BD, He XS, Zhang H, Li YH, Pu SY, Liu SJ, Yu MD, Yang C (2019) Redox properties and dechlorination capacities of landfill-derived humic-like acids. Environ Pollut 253:488–496

Xu HC, Yu GH, Yang LY, Jiang HL (2013) Combination of two-dimensional correlation spectroscopy and parallel factor analysis to characterize the binding of heavy metals with DOM in lake sediments. J Hazard Mater 263:412–421

Xu HC, Yan MQ, Li WT, Jiang HL, Guo LD (2018) Dissolved organic matter binding with Pb(II) characterized by differential spectra and 2D UV-FTIR heterospectral correlation analysis. Water Res 144:435–444

Xu HC, Zou L, Guan DX, Li WT, Jiang HL (2019) Molecular weight-dependent spectra and metal binding properties of sediment dissolved organic matter from different origins. Sci Total Environ 665:828–835

Yamashita Y, Jaffé R (2008) Characterizing the interactions between trace metal and dissolved organic matter using excitation-emission matrix and parallel factor analysis. Environ Sci Technol 42:7374–7379

Yan MQ, Wang DS, Korshin GV, Benedetti MF (2013) Quantifying metal ions binding onto dissolved organic matter using log-transformed absorbance spectra. Water Res 47:2603–2611

Yan W, Wang HB, Jing CY (2016) Adhesion of Shewanella oneidensis MR-1 to goethite: a two-dimensional correlation spectroscopy study. Environ Sci Technol 50:4343–4349

Yang X, Zhang XL, Wang ZW, Li S, Zhao J, Liang GW, Xie XY (2019) Mechanistic insight into removal of norfloxacin from water using different natural iron ore-biochar composites: more rich free radicals derived from natural pyrite-biochar composites than hematite-biochar composites. Appl Catal B Environ 255:117752

Yu GH, Tang Z, Xu YC, Shen QR (2011) Multiple fluorescence labeling and two dimensional FTIR-^{13}C NMR heterospectral correlation spectroscopy to characterize extracellular polymeric substances in biofilms produced during composting. Environ Sci Technol 45:9224–9231

Yuan DH, Guo XJ, Wen L, He LS, Wang JG, Li JQ (2015) Detection of copper(II) and cadmium(II) binding to dissolved organic matter from macrophyte decomposition by fluorescent excitation-emission matrix spectra combined with parallel analysis. Environ Pollut 204:152–160

Yuan Y, Xi BD, He XS, Tan WB, Gao RT, Zhang H, Yang C, Zhao XY, Huang CH, Li D (2017) Compost-derived humic acids as regulators for reductive degradation of nitrobenzene. J Hazard Mater 339:378–384

Zhai XQ, Li ZW, Huang B, Luo NL, Huang M, Zhang Q, Zeng GM (2018) Remediation of multiple heavy metal-contaminated soil through the combination of soil washing and in situ immobilization. Sci Total Environ 635:92–99

Zhang M, Gao B, Varnoosfaderani S, Hebard A, Yao M, Inyang M (2013) Preparation and characterization of a novel magnetic biochar for arsenic removal. Bioresour Technol 130:457–462

Zhao FJ, Zhu YG, Meharge AA (2013) Methylated arsenic species in rice: geographical variation, origin, and uptake mechanisms. Environ Sci Technol 47:3957–3966

Zhao FJ, Ma YB, Zhu YG, Tang Z, McGrath SP (2015) Soil contamination in China: current status and mitigation strategies. Environ Sci Technol 49:750–759

Zhao XT, Hu ZZ, Yang X, Cai XW, Wang ZW, Xie XY (2019) Noncovalent interactions between fluoroquinolone antibiotics with dissolved organic matter: a ^{1}H NMR binding site study and multi-spectroscopic methods. Environ Pollut 248:815–822